Review Article

Jijil JJ Nivas*, Elaheh Allahyari and Salvatore Amoruso

Direct femtosecond laser surface structuring with complex light beams generated by q-plates

https://doi.org/10.1515/aot-2019-0067
Received December 2, 2019; accepted January 30, 2020; previously published online March 5, 2020

Abstract: Direct femtosecond (fs) laser surface structuring became a versatile way to generate surface structures on solid targets demonstrating a high degree of flexibility and controllability in creating different types of structures for many applications. This approach demonstrated an alteration in various properties of the surface, such as optical properties, wetting response, etc. This paper focuses on direct fs laser surface structuring using complex light beams with spatially variant distribution of the polarization and fluence, with emphasis on the results obtained by the authors by exploiting q-plate beam converters. Although striking scientific findings were achieved so far, direct fs laser processing with complex light fields is still a novel research field, and new exciting findings are likely to appear on its horizon.

Keywords: femtosecond laser surface processing; LIPSS; optical vortex; vector vortex beams.

Classification: PACS 42.62. – b; 52.38.Mf; 61.80.Ba; 79.20.Ds; 79.20.Eb; 81.16.Nd.

1 Introduction

Lasers constitute an essential tool for a variety of materials processing approaches in scientific and industrial fields [1–4]. In many cases, the shaping of the laser beam features was demonstrated as a viable route to add further controlling parameters, increases the versatility, and expands their use in novel, interesting directions [5, 6]. Thanks to the possibilities that are already demonstrated in a variety of other applications (e.g. microscopy, quantum optics and information, photonics, optical trapping, data communication, etc.) [7–12], complex light beams with tailored intensity or polarization are attracting increasing interest also in laser surface structuring. In this context, the development of efficient beam converters that generate powerful pulses of complex light beams with tailored intensity and/or polarization patterns can facilitate or allow the fabrication of novel surface features.

The emerging field of complex (or structured) light beams deals with the topological properties of light such as beams with unconventional intensity, polarization, and phase [7]. A light beam carrying orbital angular momentum (OAM) constitutes a classical example of complex light, and it is characterized by an annular intensity spatial profile with a central singularity (null intensity) where the phase and polarization are undefined. Historically, a light field with a singularity was first predicted and detected by Pancharatnam in 1956 [13]. Ross [14] and Haldane [15] reported on uniform circularly polarized beams where the singularity comes from a helical phase profile. When referring to scalar fields, i.e. a single polarization component with singularity of the phase profile, the term 'optical vortex' (OV) is typically used. This is characterized by a definite OAM and helical phase. The OV beam represents the Laguerre-Gaussian modes with an azimuthally varying phase term $e^{i\ell\phi}$, with the integer ℓ describing the amount of OAM of the light field (in units of $\hbar$). The phase profile varies continuously around the optical axis, which leads to a helicoidal wavefront with the screw axis along the optical axis [7]. A vortex beam with vectorial or polarization singularities is referred to as a vector vortex (VV) beam with zero total OAM.

***Corresponding author: Jijil JJ Nivas,** Dipartimento di Fisica 'Ettore Pancini', Università di Napoli 'Federico II', Complesso Universitario di Monte S. Angelo, Via Cintia, I-80126 Napoli, Italy; and CNR-SPIN, UOS Napoli, Complesso Universitario di Monte S. Angelo, Via Cintia, I-80126 Napoli, Italy, e-mail: jijil@fisica.unina.it. https://orcid.org/0000-0002-9463-886X
Elaheh Allahyari and Salvatore Amoruso: Dipartimento di Fisica 'Ettore Pancini', Università di Napoli 'Federico II', Complesso Universitario di Monte S. Angelo, Via Cintia, I-80126 Napoli, Italy; and CNR-SPIN, UOS Napoli, Complesso Universitario di Monte S. Angelo, Via Cintia, I-80126 Napoli, Italy

The generation of a vortex beam with an annular profile can be accomplished in several ways, some of which are quoted hereafter. One method is the insertion of birefringent elements, axial dichroic components, wire grids, amplitude masks, etc. in the laser cavity, forcing the oscillation into higher-order modes [16–18]. An efficient generation of a Laguerre-Gaussian mode carrying OAM is obtained from a Hermite-Gaussian mode using cylindrical lenses [19, 20], but the requirement on the initial mode limits the accessibility of higher mode with OAM. Use of a diffraction grating with a bifurcation in the pattern is another approach [21]; however, it suffers from issues like low diffraction efficiency and unwanted diffraction orders. A spiral-shaped crystal with variable thickness in the azimuthal direction (spiral phase plate) [22] or optical elements with spatially variant fs laser-induced birefringence (S-plate) [23] can also allow efficient generation of a beam with OAM, but it demands very precise fabrication engineering. A versatile and alternative way that overcomes some of these issues makes use of computer-generated holograms with spatial light modulators (SLMs), thus, enabling the generation of any diffraction pattern and, in turn, any corresponding complex light field [24]. The SLMs act as tiny, precisely controlled birefringent pixel arrays that can write almost any phase profile. Finally, a new optical device capable of generating light beams carrying OAM is the q-plate developed by Marrucci et al. in 2006 at University of Naples '*Federico II*' [25]. It consists of a thin film of liquid crystal sandwiched between two transparent glasses plated with a conductive coating [26]. The q-plate essentially acts as a birefringent wave plate with an inhomogeneous distribution pattern of the local optical axis in the transverse plane. The pattern of the optical axis distribution is defined by a semi-integer topological charge q. The q-plate offers a highly efficient vortex beam generation mechanism based on spin-to-orbital conversion of the angular momentum of light. In the last years, we used various q-plates to generate fs VV laser beams in order to investigate its application to direct fs laser surface structuring. Here, we aim to illustrate a series of experimental findings that we obtained using complex light beams with spatially variant polarization and fluence distributions generated by q-plate beam converters.

Laser irradiation of a solid target (metals, semiconductors, and dielectrics) with fs laser pulses allows the generation of various types of surface structures and, more specifically, of so-called laser-induced (quasi-)periodic surface structures (LIPSSs) [1–3, 27, 28]. LIPSSs are usually classified by relating their spatial period, Λ, to the laser wavelength, λ: the classical near-wavelength-sized structures with $\Lambda \geq \lambda/2$ are termed as low-spatial frequency (LSF) LIPSSs, whereas high-spatial frequency (HSF) LIPSSs refer to $\Lambda < \lambda/2$ [2]. The most common LSF-LIPSS (LSFL) are ripples oriented perpendicular to the laser polarization. The ripples typically form at a laser pulse fluence close to the ablation threshold of the target material and are characterized by a period $\lambda/2 \leq \Lambda \leq \lambda$. In metals and semiconductors, their generation is associated to the interference occurring between surface-scattered electromagnetic waves and incident laser light, which leads to a modulation of the light intensity spatial distribution determining the imprint of a morphological pattern onto the material surface [1, 2, 27–30]. At a large number of laser pulses or for high fluence, other supra-wavelength LIPSS oriented parallel to the laser polarization, termed as grooves, are also formed [31–36], whose formation mechanisms are not yet fully clarified. However, recent theoretical and experimental investigations underline the important effects of molten material hydrodynamics [32–34] and nanoparticle back-deposition [29, 35–37] on the formation of these supra-wavelength LIPSS.

Before presenting our own results, we recall hereafter a few works addressing the historical development of laser processing with vortex beams.

The first works on surface structuring with fs pulses were done in the year 2010 with vortex beams produced using a computer-generated hologram [38], a segmented waveplate, and a uniaxial birefringent crystal [39]. In the first case, Ran et al. irradiated a Zr-based amorphous alloy foil forming a ring-shaped crater displaying ripples and 'coral-like' structures [38], while in the second one, Shen et al. used radially and azimuthally polarized beams on silicon observing a clear formation of periodic structures distributed over an annular crater [40]. For the third, Hnatovsky et al. reported on materials processing of fused silica (SiO_2) and soda-lime glass using tightly focused fs vortex pulses with $\ell = +2$ demonstrating the generation of annular craters with submicron width [39]. Successively, the same groups did extensive work revealing the properties of vortex beam ablation of fused silica [41] and silicon [42] at moderate and tight focusing conditions and addressing the formation of surface ripples following the local field structure of the spatially variant light polarization. In the same year, 2010, laser ablation of a Ta sample with nanosecond (ns) OV beams with $l = 1$ and 2 generated using a spiral phase plate was carried out by Omatsu's team at Chiba University [43]. Successively, the same group also demonstrated the fabrication of twisted metallic nanoneedles using a few (typically 2–5) ns OV pulses [44, 45]. In 2012, Kai Lou et al. reported the fabrication of complex two-dimensional subwavelength

microstructures (ripples with spatial period in the range of 670–690 nm) on silicon induced using fs VV light fields generated by a vector field-generation system [46]. Then, many other investigations followed [47–51], and a striking outcome of using VV beams in fs laser surface structuring is the elaboration of biomimetic surfaces on Ni, showing lotus leaf-like as well as shark skin-like morphologies, realized by large area scanning with radially and azimuthally polarized vector beam generated by an S-plate [52].

The first experiments on fs laser surface structuring with a VV beam generated by q-plate, with $q=1/2$, were carried out at the University of Naples and evidenced the formation of annular crater covered with a variety of micro- and nanostructures over silicon and copper targets [53, 54]. In this paper, we aim to review the variety of surface patterns and crater shapes that can be created by means of VV beams generated by q-plates, especially considering weak focusing conditions. In particular, we summarize results obtained with different q-plates characterized by topological charges ranging from $q=1/2$ to $q=5/2$ demonstrating the versatility of direct fs laser surface structuring based on such an approach. Besides the more conventional VV beams (e.g. radially and azimuthally polarized), we report other interesting beams with more intricate spatial distribution of polarization and intensity generated by adding further optical elements in the beam path, such as waveplates and polarizers as well as fascinating examples of processing with complex light fields obtained by optical retardation tuning of the q-plates. Finally, some examples of step scanning for the formation of arrays over a large area are also briefly illustrated.

2 Experimental methods

Figure 1 reports a typical setup used for direct fs laser surface structuring with the addition of a q-plate. Typically, in weak focusing conditions, laser pulses provided by an fs laser source are focused by a lens on a sample target surface. The sample is mounted on a computer-controlled translation stage, and an electromechanical shutter is generally used to select the number of laser pulses reaching the target. A variable attenuator [e.g. a half wave plate (HWP) and a polarizer] is used to vary the laser pulse energy, and an iris can be exploited to select the most intense part of the beam. Typically, in standard direct laser structuring, a beam with a Gaussian profile is used (see Figures 1 and 2A, left). The direction of the linearly polarized input Gaussian beam entering the q-plate is controlled by another HWP. In our case, the insertion of a q-plate, which is a planar optical element, allows a facile way to generate a variety of VV beams and exploit them for direct laser surface structuring of the sample. The top in Figure 1 displays the images of the q-plates taken through two cross-polarizers with symmetric lobes whose number is related to the q value.

A q-plate essentially works as an inhomogeneous birefringent linear retarder characterized by a distribution pattern of the local optic axes in its transverse x–y plane [25]. The q-plate cell has a homogeneous thickness providing a uniform optical retardation δ point by point along the plate, whose value is controlled by an external electric voltage [55]. The q-plate transforms the input light field, described by the Jones vector $\boldsymbol{\psi}_{\text{in}}(x, y)$ at any position (x, y) into an output light field $\boldsymbol{\psi}_{\text{out}}(x, y)$ given by:

$$\boldsymbol{\psi}_{\text{out}}(x, y)=\left[\cos\left(\frac{\delta}{2}\right)I-i\sin\left(\frac{\delta}{2}\right)M_q(\alpha)\right]\boldsymbol{\psi}_{\text{in}}(x, y) \tag{1}$$

where I is the identity matrix, and $M_q(\alpha)$ is the Jones matrix of a half-wave plate whose axis forms an angle $\alpha(x, y)$ with respect to the reference x-axis. The local optic axis is oriented with respect to the x-axis at an angle α that in polar coordinates (r, ϕ) is given by the equation:

$$\alpha(r, \phi)=q\phi+\alpha_0 \tag{2}$$

with the azimuthal angle $\phi=\text{arcotg}\left(\frac{y}{x}\right)$, the radial coordinate $r=\sqrt{x^2+y^2}$, and the initial orientation angle at $y=0$ given by α_0. The center in Figure 2A reports an image of q-plates kept in between to cross-polarizing sheets showing the azimuthal variation of a q-plate birefringence.

Equations (1) and (2) show that the output beam depends on both the value of the topological charge, q, and the optical retardation, δ. In particular, for any given q-plate with a fixed value of q, δ acts as a tuning parameter between two limiting states. The details about q-plate voltage tuning and the associated optimization of the output beam can be found elsewhere [56]. Briefly, the tuning of the q-plate optical birefringent retardation, δ, is achieved by varying peak-to-peak value, V_{pp}, of the driving voltage applied between the two conductive parallel faces of the q-plate, which is a square wave optimized at 11 kHz [10, 25, 55, 57]. For $\delta\approx 2\pi$ (un-tuned condition), the q-plate behaves as a transparent medium that leaves the input beam unchanged. At $\delta\approx\pi$ (optimal tuning), a half-wave retardation condition occurs, and a vectorial beam with an OAM $\ell=\pm 2q$ is achieved as the output [26]. This beam presents a spatial distribution with a central region of null intensity (due to undefined phase on the beam axis), a principal intense annulus, and several secondary rings at increasing radial distance from the beam axis [10, 58]. In the experiments, the principal intense annular beam is selected by the iris (see Figures 1 and 2B) obtaining a vortex beam, as sketched in the right of Figure 2A.

In the case of an input beam with circular polarization, the q-plate generates a circularly polarized OV beam with a helical profile. The spiral phase of the OV beam rotates about the optical axis that causes the wavefront of the light to twist like a corkscrew as it propagates. The topological charge q of the q-plate determines the number of twists occurring in one wavelength propagation distance. The positive or negative sign of q defines the handedness of the twist in the left (anticlockwise) or right (clockwise) direction.

In our experiments, we typically shine a tuned q-plate ($\delta\approx\pi$) with a Gaussian beam linearly polarized along the reference (horizontal) x-axis, then we can consider $\boldsymbol{\psi}_{\text{in}}(x, y)=\boldsymbol{G}_H(x, y)$. In tuned conditions ($\delta\approx\pi$), the output beam is $\boldsymbol{V}_q(x, y)=-iM_q(\alpha)\boldsymbol{G}_H(x, y)$ that, except for the multiplicative phase term $-i=e^{-i\frac{\pi}{2}}$, is a superposition of the left and right circularly polarized helical beams with opposite OAM $\ell=\pm\ 2q$ and a spatial distribution expressed in cylindrical coordinates, as:

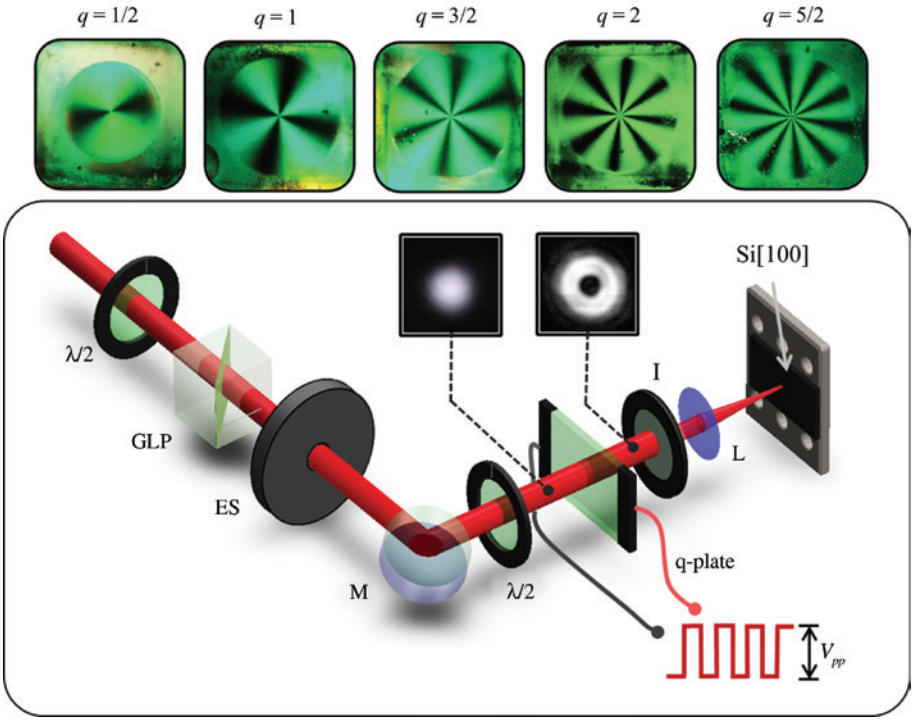

Figure 1: Diagram of the typical experimental setup used for fs laser surface structuring. The insertion of a q-plate allows structuring with VV beams. λ/2 = half-wave plate; GLP, polarizer; ES, electro-mechanical shutter; I, iris; L, lens. The silicon target is fixed on a computer-controlled high-precision three-axis translation stage. The square wave of V_{pp} (peak to peak) denotes the driving signal to the q-plate. The CCD images of the beam before and after the q-plate are reported in the respective positions. Top: the images of the q-plates taken through two cross-polarizers, from where the respective q values can be found from the count of symmetric lobes.

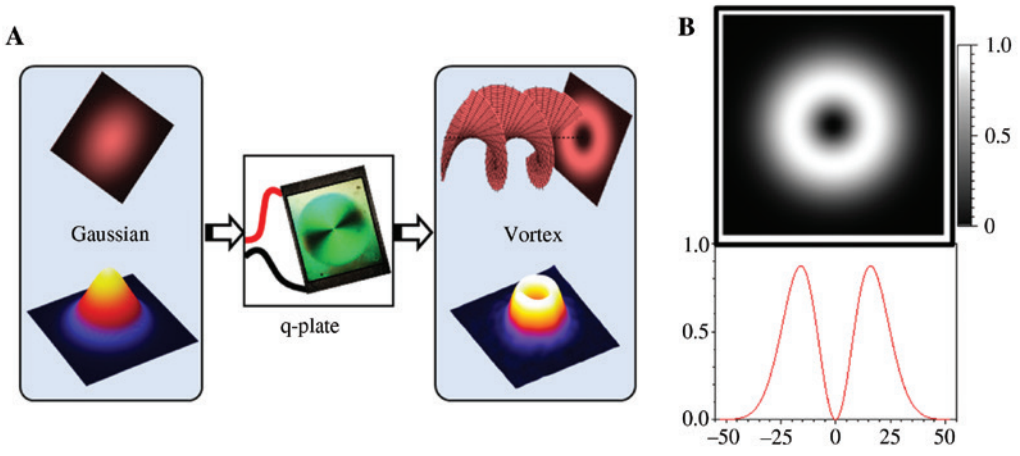

Figure 2: (A) Schematic representation of the conversion of Gaussian beam to a vortex beam with OAM by a q-plate of $q = 1/2$. (B) The annular profile of the vortex beam (top) and the linear profile taken along the diameter (bottom).

$$\boldsymbol{V}_q(x, y) \propto f_\ell(r, z)(\boldsymbol{e}_l e^{i|\ell|\phi} + \boldsymbol{e}_r e^{-i|\ell|\phi}) \tag{3}$$

where $\boldsymbol{e}_l$ and $\boldsymbol{e}_r$ are the unit vectors associated with the left and right circular polarization states and z the direction of the propagation axis. The function $f_\ell(r, z)$ describes the radial distribution of the field and is identical for the two modes carrying opposite values of the OAM, $\pm|\ell|$. The temporal dependence is not shown in Eq. (3) because it is related to the temporal profile of the input laser pulse and defines a global term not affecting the spatial and polarization structure. In general, at the exit of a tuned q-plate, i.e. at an optical retardation $\delta \approx \pi$ [see Eq. (2)], the profile of the generated VV beam is described by a hyper-geometric Gaussian mode [59, 60]. However, the output beam profile is well approximated by a Laguerre-Gauss mode sub-class $LG_{0,\ell}$ after filtering with a circular aperture [11]. Hence, using

q-plates with different topological charges, a variety of VV beams with different polarization states and a null total OAM can be generated and used for direct laser surface structuring, as will be illustrated in Section 3.

Interestingly, the q-plate offers even more versatility. In fact, by selecting values of the optical retardation different from the tuned ($\delta \approx \pi$) and un-tuned ($\delta \approx 2\pi$) conditions, the q-plate generates a superposition state of the $\boldsymbol{G}_H$ and $\boldsymbol{V}_q$ light fields given by:

$$\boldsymbol{\psi}_{\text{out}}(x, y) = \cos\left(\frac{\delta}{2}\right)\boldsymbol{G}_H(x, y) - i \sin\left(\frac{\delta}{2}\right)\boldsymbol{V}_q(x, y) \quad (4)$$

For each value of q, Eq. (4) shows that it is possible to obtain a variety of complex VV beams, of which $\boldsymbol{G}_H(x, y)$ and $V_q(x, y)$ are the two degenerate cases, characterized by a quite complex spatial variation of the polarization and fluence distribution [see Eq. (4)]. Hence, by tuning the optical birefringent retardation of the q-plates, δ, optical vector beams with a composite intensity distribution can be produced that can eventually lead to the generation of surface structures with a rather complex distribution of ripples and grooves and crater shapes, as illustrated below in Section 4.

The surface structuring experiments discussed hereafter were carried out by focusing the beams generated by the q-plate, in the different tuning conditions illustrated above, on the surface of an intrinsic (100) silicon target, in air, with a selected number of laser pulses, N. The input beam to the q-plate was a Gaussian laser beam with a pulse duration of $\approx$35 fs at a central wavelength of 800 nm provided by a Ti:Sa fs laser source. Silicon was selected as the target material because it is a typical case study semiconductor material with widespread applications (e.g. in mechanical, optical, and electronic devices) that supports a variety of surface structures and the formation of well-pronounced LIPSS [1, 61]. Moreover, the direct relationship between the LIPSS orientation (ripples perpendicular and grooves parallel to it) provides a facile, direct visualization of the local polarization direction allowing to gain a map of the state of polarization of the VV beam imprinted on the target surface. In addition, it is easily obtained as a crystal, thus providing a very high-quality pristine surface making it an ideal candidate for the fs laser-processing studies with very limited influences of the original state of the sample surface. In our studies, we typically used intrinsic (100) silicon targets with a resistivity larger than 200 Ω cm and a thickness of about 400 μm. Finally, it is worth mentioning that in all the experiments, we used weak focusing conditions that ensure a good imprinting of the features of the beam on the surface of the material and a clear identification of the generated surface structures.

3 Surface structures produced with VV beams generated by tuned q-plates

In this section, we illustrate the surface structures produced by electrically tuning the q-plates to the standard optical retardation of $\delta \approx \pi$, thus achieving annular VV as output beams. We discuss first the surface structures obtained with beams generated by the basic q-plate with a topological charge $q = 1/2$. The most well-known beams of this family are radially or azimuthally polarized beams, which because of their cylindrical symmetry are also indicated as basic examples of cylindrical vector beams [11, 26]. These states of polarization are generated by the basic q-plate with a topological charge $q = 1/2$ for an input beam with vertical or horizontal polarization [26].

Figure 3A reports a typical example of the SEM micrograph of the silicon surface after irradiation with a radially polarized VV beam, for $N = 100$ pulses with an energy $E \approx 50$ μJ (peak fluence $\Phi_p \approx 0.5$ J/cm^2). For comparison, Figure 3B shows the SEM micrograph of the sample surface obtained in the same experimental conditions for the circularly polarized OV beam. In both cases, the shallow annular crater formed on the sample reflects the beam shape. The insets in panels (C) and (D) report zoomed views of regions located at the external (red) and internal (blue) crater boundaries giving a more detailed visualization of the surface morphological features. One can clearly observe the formation of a central structure made by an assembly of nanoparticles in the region irradiated by the inner part of the beam with almost null intensity (see e.g. Figure 2B). A layer of nanoparticles is also present in the outer area surrounding the crater. This shows that random nanoparticle-assembled nanostructures form in the central and external regions where the local fluence of the beam is lower than the material ablation threshold. In the case of the radially polarized VV beam (see Figure 3A and C) micron-sized grooves, aligned along the local polarization of the VV beam, cover the most part of the annular crater. This grooved region is surrounded by two adjacent areas decorated by subwavelength ripples directed perpendicular to the local laser polarization. The presence of rippled and grooved areas separated by a sharp transitional region evidences the existence of a clear threshold for the formation of grooves, in agreement with the experimental findings obtained using Gaussian, linearly polarized laser beams [35]. In the case of the circularly polarized OV beam, with a non-zero OAM, (B) and (D) of Figure 3 do not evidence the formation of clear periodic features. Instead, the surface is mainly covered by shallow columnar features, randomly oriented, as well as complex network-like structures. In particular, close to the outer boundary of the crater, i.e. in the region of low beam intensity, clear bumps with a subwavelength size are found, and no signature of ripples can be recognized, similar to the results obtained in the case of a circularly polarized Gaussian beam [62]. However, the area close to the spot center evidences some minor formation of texture resembling ripples and grooves but without any specific directionality. In both conditions, the outer region of the structured spot is densely covered with collections of

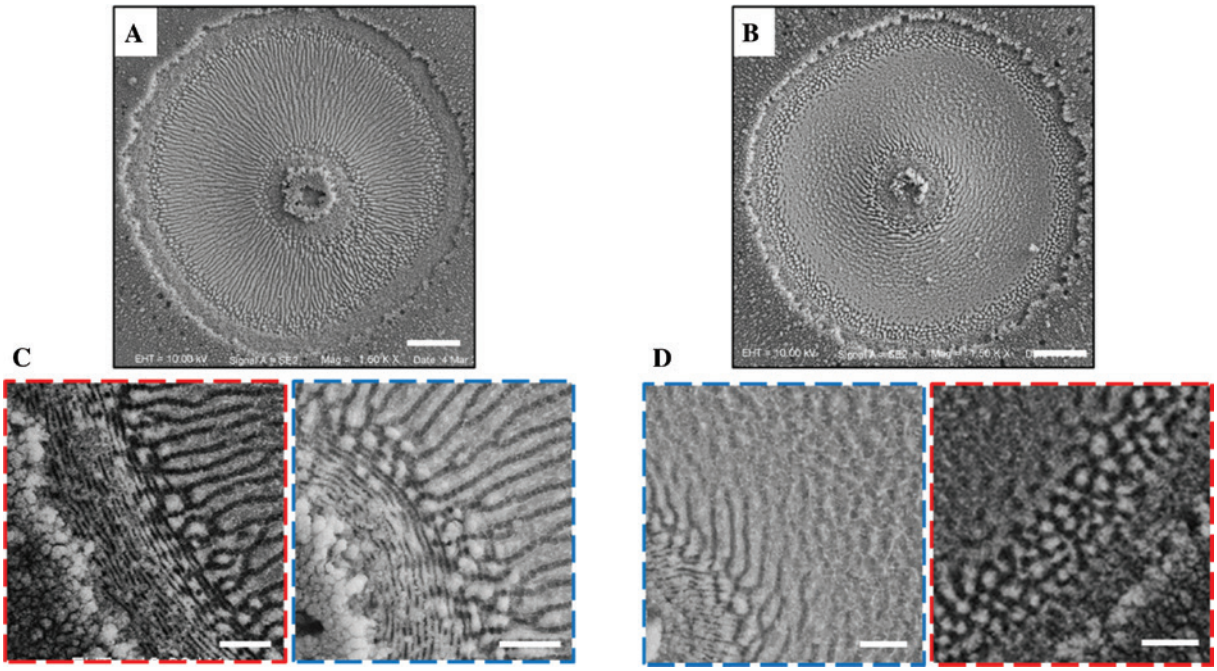

Figure 3: Surface structures generated on the silicon surface with a VV beam (A) and OV (B) after an irradiation sequence of $N=100$ pulses with an energy $E\approx 50$ μJ. (C) and (D) Zoomed views exemplifying the surface morphological features present at the external (red dashed squares) and internal (blue dashed squares) boundary regions of the shallow crater. The scale bars are (A, B) 20 μm and (C, D) 5 μm.

nanoparticles. It is worth mentioning that no effect of OAM and related helical phase of the beam can be addressed at the level of focusing of fs OV pulses used in our experimental conditions.

Besides the two cases of Figure 3, there are several other states of polarization for the VV beams generated using a q-plate with $q=1/2$, such as azimuthal, spiral, linear, and mixed states. Some examples of SEM images of the silicon surface illustrating the complex surface patterns generated by fs VV laser pulses with different states of polarization are displayed in Figure 4. In particular, (A) and (B) report azimuthal and spiral polarizations, while (C), (D), and (E) refer to linear and mixed polarization states of the VV beam generated by means of an additional quarter wave plate after the q-plate. The irradiation sequence is again with $N=100$ pulses at an energy $E\approx 50$ μJ. The resulting surface presents various annular regions characterized by different surface morphologies inside the annular crater. This consists again of an inner ring-shaped region characterized by micron-sized grooves, preferentially aligned along the local beam polarization, surrounded by adjacent areas with ripples perpendicular to the local laser polarization. Zoomed views of the non-ablated crater center surrounded by ripples are displayed in the inset of (A–C); meanwhile, (D–F) show the surface morphology after irradiating with complex VV beams generated by passing the radial and azimuthal beam, respectively, through a quarter wave-plate, generating a mixed state of polarization, before focusing. The far-field intensity and polarization patterns of the corresponding VV beams are shown in the lateral insets. All the experimental findings indicate that the formed LIPSS are strictly linked to the local polarization of the VV beam, hence, suggesting that a large variety of patterns can be designed already by means of the basic q-plate with $q=1/2$ or simply adding to it a wave-plate.

We turn now to illustrate the results of surface structuring with fs VV beams generated by q-plates with higher values of q that are characterized by a more complex spatial distribution of the polarization in transverse plane. Some examples are summarized in Figure 5 for beams generated by q-plates with $q=1$, 5/2, and 2, in tuned conditions ($\delta\approx\pi$). The number of pulses and energy of the irradiation sequence are $N=200$ and $E\approx 50$ μJ for $q=1$ and $N=200$ and $E\approx 100$ μJ for $q=2$ and 5/2. For the cases of $q=1$ and $q=5/2$, zoomed views of the surface structures are shown in (B) and (D), respectively, together with the corresponding maps of the beam, while (E) displays the surface morphology for the VV beam generated with $q=2$. These examples clearly demonstrate that also for larger q-values and more complex polarization patterns, the surface structures are spatially arranged according to the local orientation of the polarization, thus allowing imprinting rather complex textures on the sample surface.

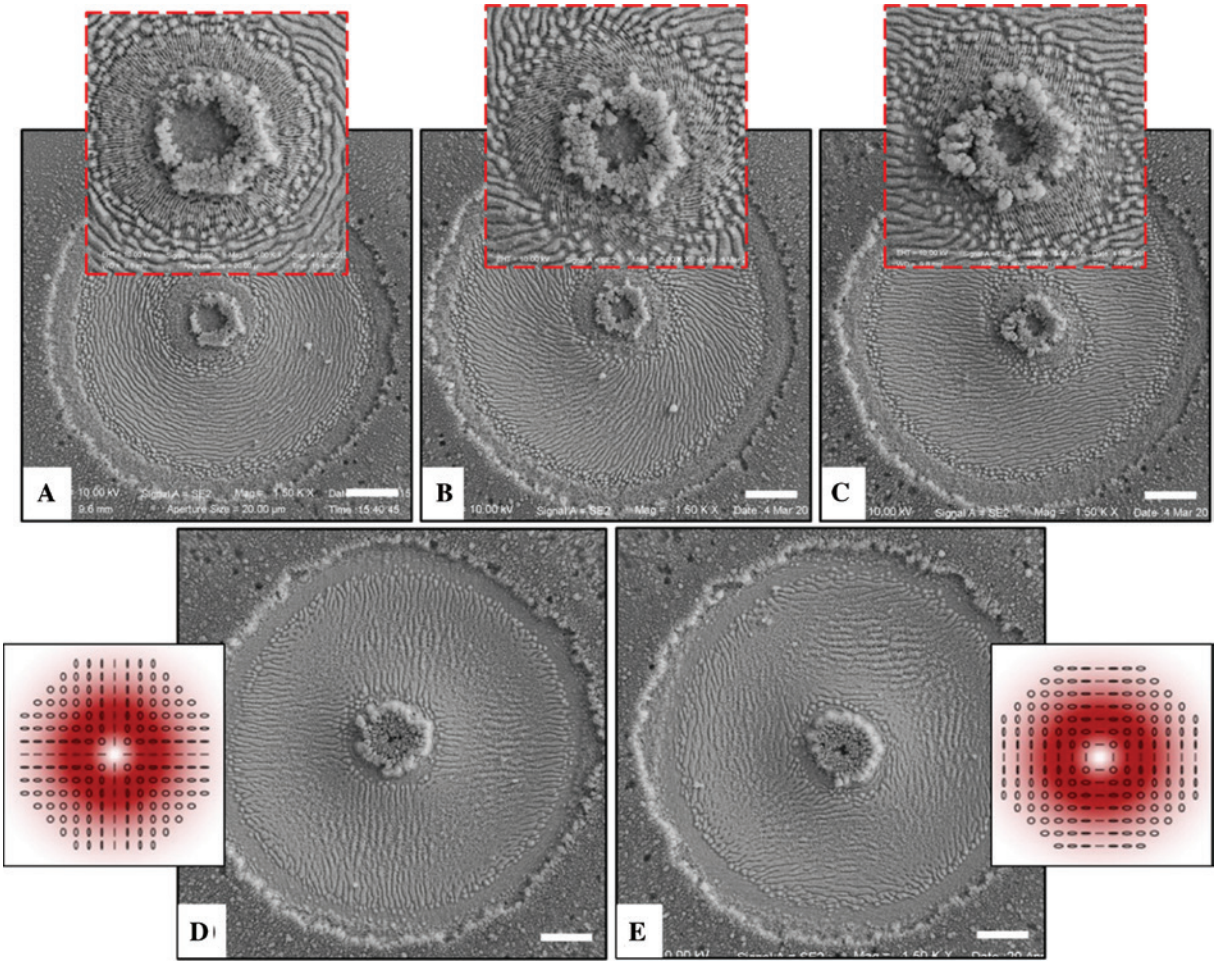

Figure 4: SEM images of the craters produced with VV beams generated by an optimally tuned q-plate ($\delta \approx \pi$) with $q = 1/2$ with a different state of polarization. (A) and (B) Azimuthal and spiral polarizations, respectively. (C–E) SEM images corresponding to linear and mixed polarization states of the VV beam generated by means of an additional quarter wave plate. In each condition, the surface is irradiated with $N = 100$ pulses at $E \approx 50$ μJ. Top insets: zoomed views of the central region for azimuthal (A), spiral (B), and linear (C) polarizations. (D, E) Lateral insets: the intensity and polarization maps of the VV beams with mixed polarization states. (A–E) Scale bars equals 20 μm.

In all the cases analyzed above, the VV beams produce craters with an annular shape resembling their intensity distribution with actual values of external and internal radii depending on the specific value of the pulse energy used. However, the relative fraction of the central non-ablated region shows a clear increase with the topological charge q of the q-plates. This aspect was addressed in detail earlier by monitoring the variation of the ratio between the internal and external radii of the annular crater [63]. Moreover, the average values of the spatial period of ripples and grooves measured in the SEM images of the craters do not show any strong dependence of the q-value resulting always in the same range, typically (535 ± 36) nm and (1.7 ± 0.2) μm for ripples and grooves, respectively, in our experimental conditions. It is worth noticing that the period LIPSS varies with experimental parameters like wavelength, pulse number, and fluence [28, 32, 64, 65]. For example, by irradiating a silicon sample with 430 fs, 800 nm pulses, Tsibidis et al. observed ripples with a period in the range of 720–740 μm [28], at a fluence of about 0.4 J/cm^2 that progressively reduces for N varying from 2 to 8. In a successive study, grooves with a period in the range of 2.5–3.5 μm [32] that gradually increases for N going from 20 to 100 at a fluence of about 0.7 J/cm^2 were reported. In one of our previous work [65], we compared the dependence of ripple and groove periods formed on silicon irradiated by Gaussian and VV beams provided by the same Ti:Sa laser system on experimental parameters like energy and number of pulses observing rather similar trends and values of the periodicity.

The strict relationship between directionality of the surface structures and the laser beam polarization allows obtaining a direct visualization of the state of polarization of intense VV beams with an adequate level of spatial

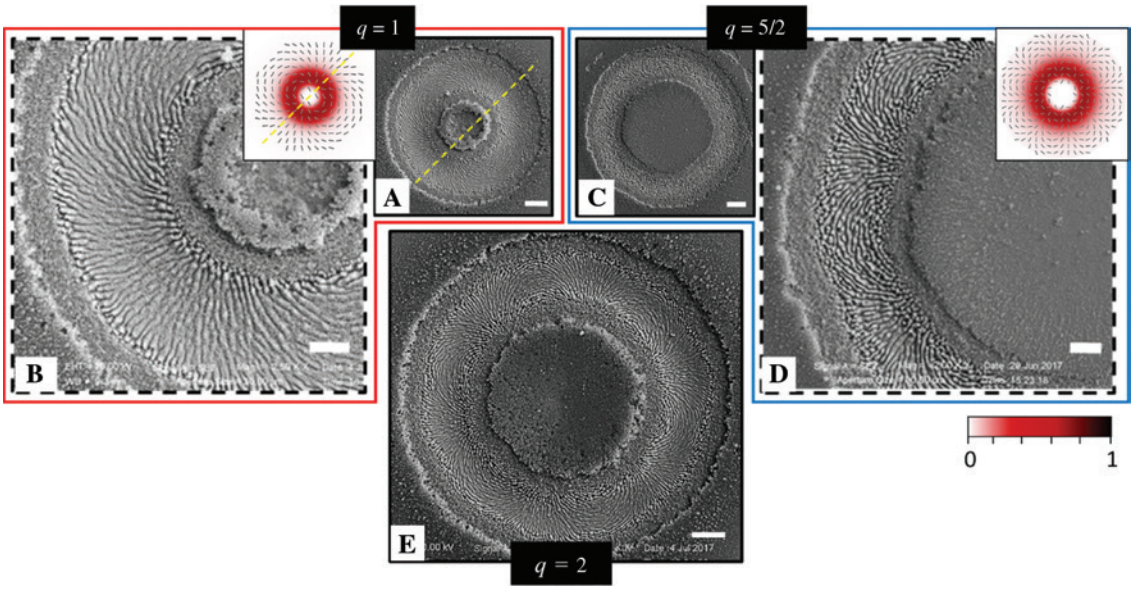

Figure 5: (A, C, E) SEM images of the surface morphologies developed on the silicon target after an irradiation sequence of $N = 200$ pulses with VV beams generated by q-plates with (A) $q = 1$, (C) $q = 5/2$, and (E) $q = 2$, respectively, in tuned conditions ($\delta \approx \pi$). The pulse energy is $E \approx 50$ μJ for $q = 1$, $E \approx 100$ μJ for $q = 2$ and 5/2. (B, D) Zoomed views of the SEM image of (A) and (C), respectively. (E) is added to represent a condition in which q value is in between that of (A) and (C). The scale bars in SEM images are (A, C, E) 20 μm and (B, D) 10 μm. (B, D) Inset: simulation of far-field beam profile with local direction of the beam polarization. In the maps, each beam intensity profile is normalized to its own maximum value as shown in the color bar.

resolution and good accuracy. This is particularly straight for the grooves, thanks to the fact that they orient directly along the local polarization of the beam; however, also the ripples can be reliably used in the region of the beam at lower fluence. Moreover, the dependence of the type of surface structure on the laser pulse fluence and number of pulses may also provide a qualitative understanding of the beam spatial intensity and topological charge, as discussed in Ref. [63].

Further possibilities in direct surface structuring can be achieved by inserting additional optical elements in the beam path from the q-plate to the focusing lens. Hereafter, we show the case of a simple linear polarizer performing polarization filtering of the VV beams. Figure 6 shows some examples of the structured surface when filtering the VV beam, in tuned conditions, with a linear polarizer transmitting only the parts of the beam that are horizontally polarized. The resulting surface features formed in the case of $q = 1$, 2 and 5/2 are composed of 4, 8, and 10 lobes as shown in (C–E) of Figure 6. Hence, this method allows generating a multi-spot pattern in the focal plane with $4q$ intense lobes, thanks to the spatially varying polarization distribution associated to the topological charge q. Such kind of laser beams can be of interest in various applications like, e.g. multi-pixel transfer of material in direct write laser techniques, mask-free subtractive printing through localized ablation, etc. [4, 5, 66].

4 Surface structures generated by means of optical retardation tuning

Here, we illustrate how the possibility of generating unconventional shapes by tailoring the laser intensity profiles through the tuning of the q-plate optical retardation δ can offer a viable route to the creation of a variety of structured light fields by coherent superimposition of the VV light field corresponding to tuned condition, $\boldsymbol{V}_q$, with the input Gaussian light field, $\boldsymbol{G}_H$ [63, 67]. The fractional contributions of the two beams is defined by the value of δ, as addressed in Eq. (4) above, and can be simply controlled by means of the amplitude of the voltage signal applied to the q-plate.

Figure 7 reports various examples of the VV beam characteristics, for q-plates with $q = 1/2$ and $q = 1$, displaying two-dimensional maps of the spatial distribution of polarization (ellipses) and fluence (in false color) for different values of δ. It is worth noting that the polarization ellipses indicating the local polarization in each position of the beam are very narrow, that is, the polarization is approximately linear and well approximated by a segment whose orientation indicates the dominant local component. The bottom of Figure 7A and B reports SEM images of the silicon sample after an irradiation sequence of $N = 200$

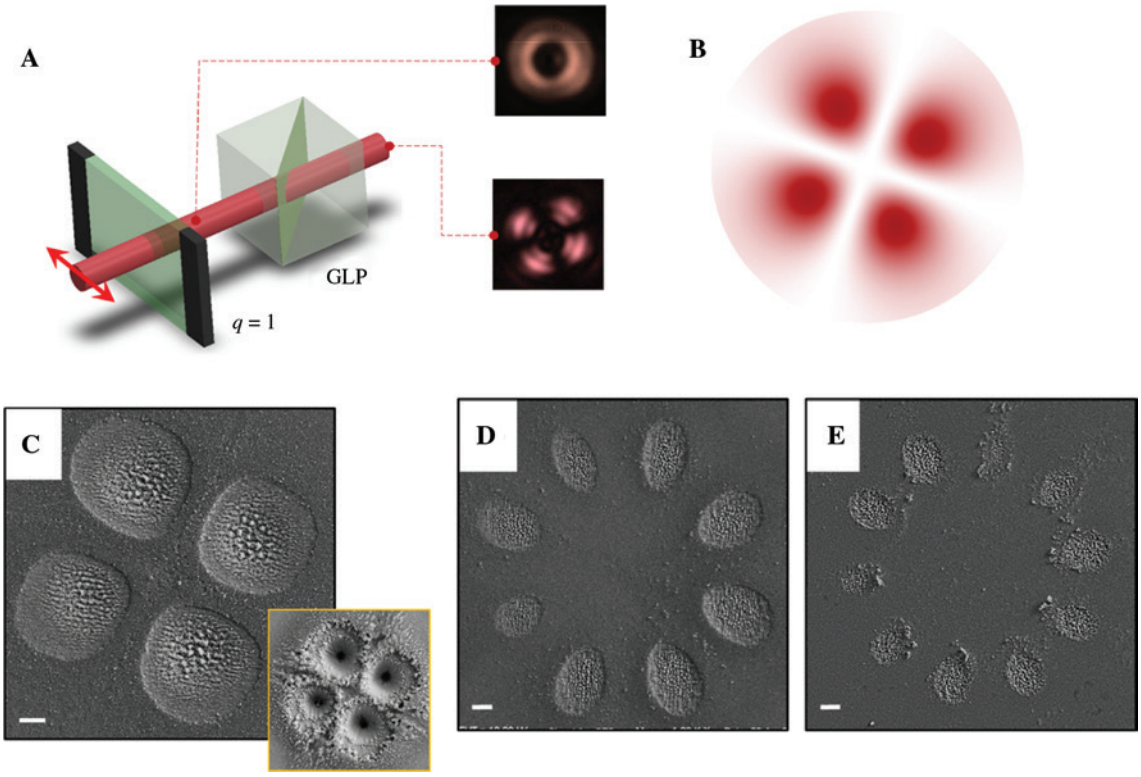

Figure 6: (A) The optical scheme including the q-plate and polarizer (GLP) for the generation for a multi-spot patterned beam with the corresponding beam profiles. (B) An example of intensity map of the VV beam for $q=1$ after filtering with a linear polarizer transmitting the horizontal polarization, which illustrates the formation of a multi-spot pattern at the focal plane. (C) SEM image of the surface pattern produced by the beam reported in (A) and (B), for $N=50$ and $E\approx 40$ μJ; inset: the surface morphology achieved after $N=500$ pulses. (D, E) SEM images of surface patterns produced by VV beams filtered by a polarizer for $q=2$ ($N=100$ and $E\approx 70$ μJ) and $q=5/2$ ($N=200$ and $E\approx 50$ μJ). (C–E) The scale bars are 20 μm.

laser pulse, at an energy $E\approx 45$ μJ for $q=1/2$ (A) and $E\approx 40$ μJ for $q=1$ (B), showing that the surface closely reflects the variation of the fluence distribution of the various fs VV beams. The tuned condition at $\delta\approx\pi$ is also reported as reference in both cases. Considering first the case of $q=1/2$ in Figure 7A, the maps show that the change in δ results in a shift of the position of the region of minimum fluence of the beam along the q-plate axis, which in the present case is horizontal. In particular, for $\delta\approx 1.51\pi$ and $\delta\approx 0.54\pi$, the region of minimum fluence is located off axis at the two opposite sides with respect to the beam center, respectively. The corresponding SEM images evidence the formation of an island of non-ablated material decorated with nanoparticles surrounded by a variety of surface structures depending on the local value of the fluence and state of polarization. For $\delta\approx\pi$, the crater is, instead, symmetric, and the grooves follow the azimuthal polarization of the $\boldsymbol{V}_q$ beam, while at $\delta\approx 2\pi$, the input $\boldsymbol{G}_H$ beam and the corresponding crater are recovered. Passing to $q=1$, one can observe that there are two regions of minimum fluence, as displayed in the maps of Figure 7B. Correspondingly, the SEM images show that the central non-ablated region gradually transforms into an ellipse and successively splits into two islands, moving in opposite directions, as the optical retardation δ is progressively tuned off from the value of π. Moreover, the morphology of the crater follows the spatial distribution of the fluence, while the surface structures reflect the local polarization states of the VV beam characterized by asymmetric patterns. Therefore, the fs VV beams with inhomogeneous spatial distribution generated by this method can provide a viable route to fabricate complex and surface patterns easily tunable by selecting rather a few control parameters as δ, N, and E.

Interestingly, the number of regions of minimum fluence depends on the value of q, being equal to $|\ell|=2|q|$. This allows further possibilities as summarized in Figure 8, which reports some examples of the intensity and polarization patterns (bottom) and corresponding SEM images (middle) of the sample surface for VV beams generated using $q=1/2$, 1, 3/2, and 5/2 for δ of about 0.8π. The top of Figure 8 displays a zoomed view of the craters. Besides the cases shown in (A) and (B), also discussed

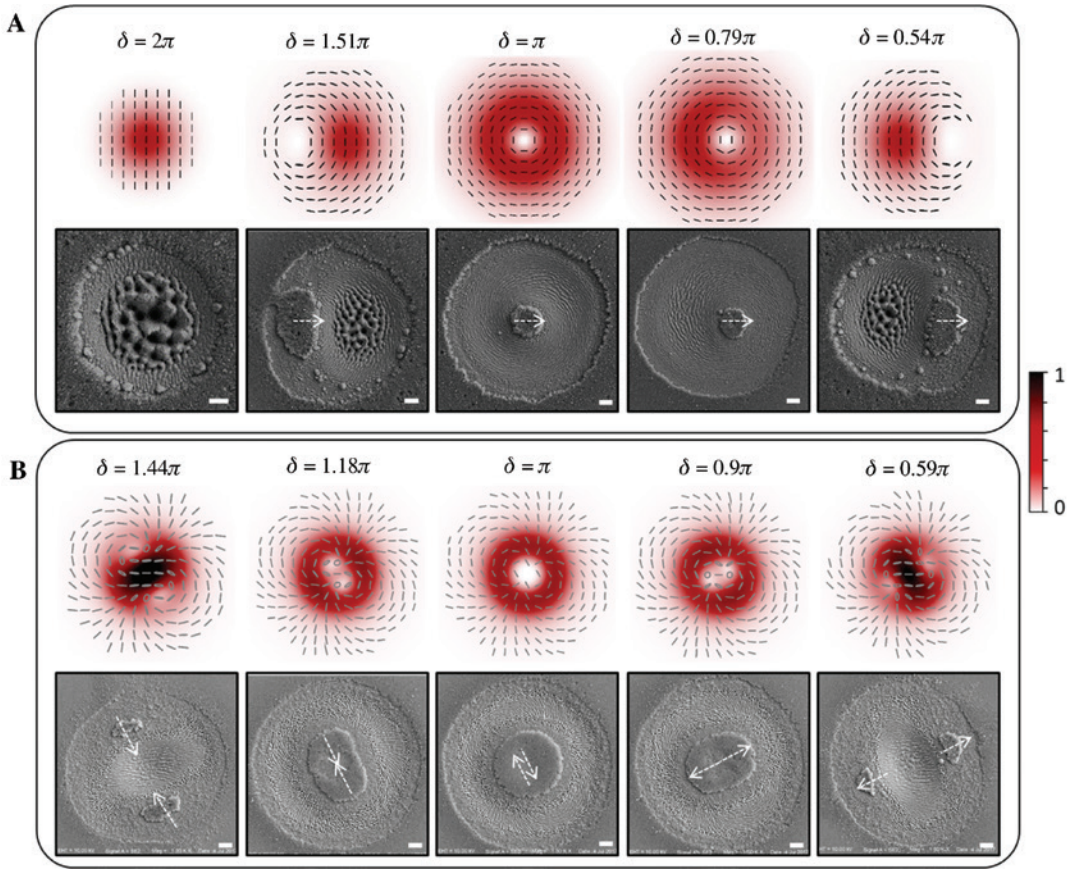

Figure 7: Examples of VV beams and surface structures produced by optical retardation tuning δ for two different q-plates with (A) $q=1/2$ and (B) $q=1$. In both cases, also the tuned beam at $\delta \approx \pi$ is reported for comparison. Top: the intensity and polarization distribution of the VV beam as a function of δ. Bottom: the SEM images of the silicon surface corresponding to irradiation with the VV beams with $N=200$ laser pulse at an energy $E \approx 45$ μJ for $q=1/2$ (A) and $E \approx 40$ μJ for $q=1$. In each SEM image, the dotted arrows mark the direction along which the regions of minimum intensity of the VV beam move while varying the optical retardation δ. The scale bar shown in the SEM images are equal to 10 μm.

above and provided here for $\delta \approx 0.8\pi$ for the sake of completeness, (C) addresses the formation of three elliptical islets located at 120° from each other for $q=3/2$. In this case, a central nearly triangular area is recognized with characteristic horizontal grooves indicating the dominant contribution of the $\boldsymbol{G}_H$ component in that area of the beam spot. In the weak focusing conditions used here, such an effect of island formation and translation can be clearly recognized up to the case of $q=3/2$. For the case of $q=5/2$ (see Figure 8D), even if five regions of minimum fluence are clearly seen in the beam profile, the crater formation by progressive material removal during irradiation does not bring to the creation of five separated islands but to a ring of unablated material with an external diameter ≈ 104 μm and a width ≈ 32 μm. This can likely happen because of the following two reasons. First, at a high q-value and a large number of singular points with lower fluence, the forming islands can overlap enough eventually merging to give rise to a single annular disk ablated in the center. Second, the increase in the beam intensity at the center as q increases to larger values leads to a corresponding larger ablation from the central region; the ablated material can be re-deposited back over the adjacent areas where the beam fluence is comparatively less, as seen earlier for lower q-values, thus reducing and eventually removing the separation between the islets left in the region of minimum fluence. Moreover, as shown in Figure 8D, the ablated annular ring presents ripples and grooves oriented forming a pattern rather similar to that observed for the $\boldsymbol{V}_q$ component at $\delta \approx \pi$ but with the central ablated part of the crater decorated with a texture of horizontal grooves evidencing the predominance of the $\boldsymbol{G}_H$ component in that region. So, in such cases of larger detuning, the beam presents a spatial structure in which the two components, i.e. $\boldsymbol{V}_q$ and $\boldsymbol{G}_H$, are rather spatially separated and can be visualized in the same spot.

Finally, we address the possibility of generating craters with rather unconventional shapes by appropriately

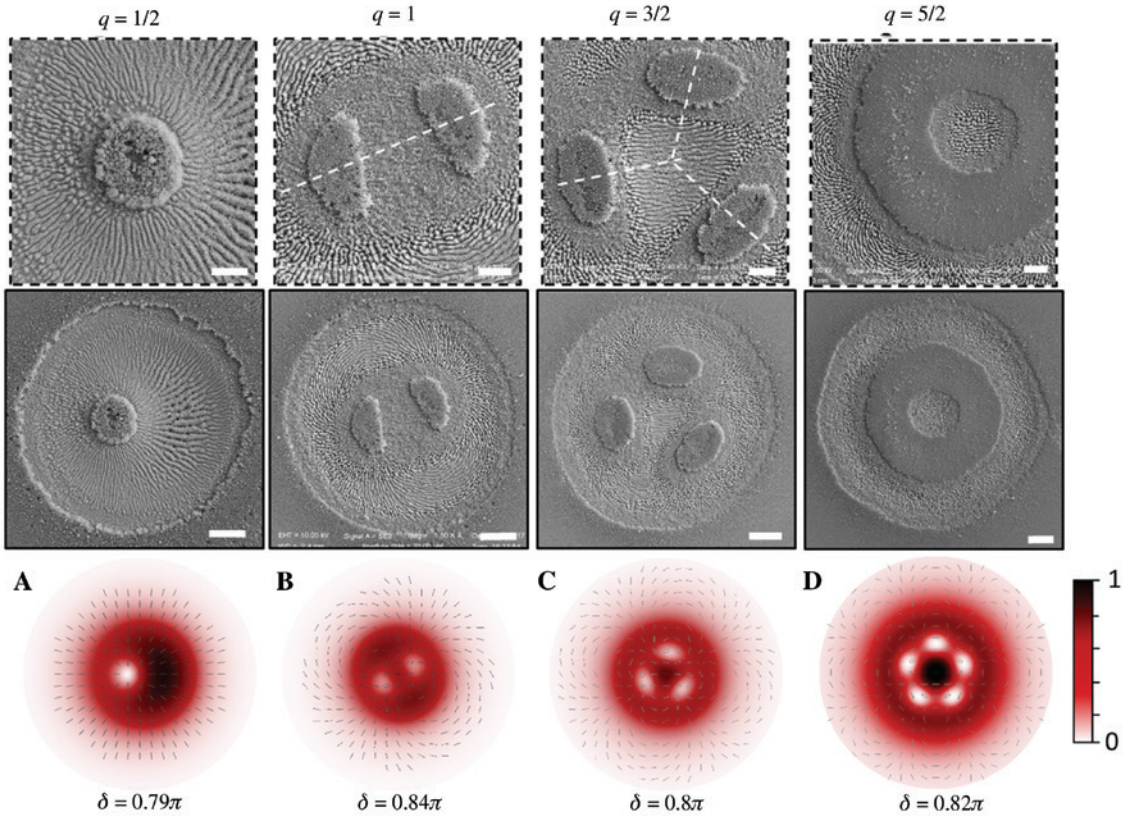

Figure 8: Bottom: The spatial distribution of light field intensity and polarization in the case of q-plate with (A) $q=1/2$, (B) $q=1$, (C) $q=3/2$, and (D) $q=5/2$ all tuned around to $\delta\approx0.8\pi$. The exact value of retardation δ can be found in each panel. Top and middle: SEM images and the zoom view of the silicon surface for the corresponding irradiation condition with number of laser pulses $N=200$, pulse energy $E\approx45$ μJ. The scale bars are 20 μm (top) and 10 μm (middle).

tailoring the laser beam intensity profile through the variation of the q-plate optical retardation. The shaped craters are decorated with peculiar textures associated to the spatial distribution of the state of polarization and fluence of the VV beam. Some typical examples are reported in the SEM images of Figure 9 for q-plates with different values of the topological charge q. All the cases correspond to an irradiation sequence of $N=200$ pulses. Figure 9A shows a lopsided crater, resembling a half-moon shape, formed by irradiation with a VV beam generated by a q-plate with $q=1/2$ at $\delta\approx1.51\pi$ with an energy $E\approx30$ μJ. A close examination of the crater evidences various surface structures including ripples, well-developed grooves, and shattered grooves that gradually appear going from the crater edges toward the region corresponding to the more intense part of the beam. Figure 9B reports the SEM image of a crater obtained with $q=1$ at $\delta\approx0.8\pi$ for pulse energy $E\approx20$ μJ. In this case, the crater resembles a bowtie shape internally decorated with ripples and grooves. For $q=3/2$, $\delta\approx0.5\pi$, and a pulse energy $E\approx20$ μJ (see Figure 9C), the surface pattern is composed of three individual, arc-shaped, ablated lobes decorated mainly with ripples, located on a circular track at ≈120° from each other, surrounding a triangular-shaped region produced by the intense part of the beam that is relatively deep and rich in columnar structures. Figure 9D shows the surface pattern generated for $q=2$, at $\delta\approx1.4\pi$ and $E\approx55$ μJ, formed by a central crater surrounded by four elliptical ablated regions located at the vertices of a square. Last, in Figure 5E, for $q=5/2$, $\delta\approx1.28\pi$, and $E\approx100$ μJ, an interesting paddle wheel-like feature with five arms and a central pentagonal-shaped hole occurs. Such examples clearly demonstrate the versatility of this approach for the generation of peculiar patterns that can also benefit from the property that their orientation in the surface plane can be controlled by means of the input beam polarization direction.

5 Fabrication of large-area arrays by step scan approach

The several patterns seen above can be easily replicated by step scanning to fabricate arrays covering larger areas of the target surface. As an example, we address here such a possibility by displaying the fabrication of few simple

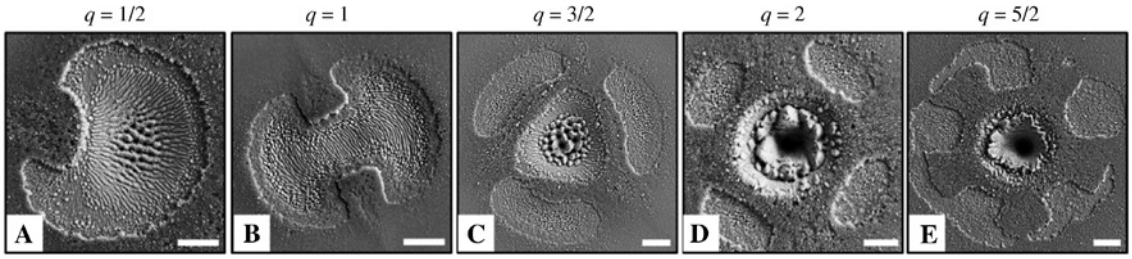

Figure 9: Examples of SEM images showing striking surface patterns generated on silicon with complex light fields obtained by optical retardation tuning of the q-plate: (A) $q=1/2$, $\delta\approx1.51\pi$, and $E\approx30$ μJ; (B) $q=1$, $\delta\approx0.5\pi$, and $E\approx20$ μJ; (C) $q=3/2$, $\delta\approx1.51\pi$, and $E\approx65$ μJ; (D) $q=2$, $\delta\approx1.4\pi$, and $E\approx55$ μJ; (E) $q=5/2$, $\delta\approx1.28\pi$, and $E\approx100$ μJ. In all cases, the number of pulses is $N=200$. All the scale bars are 20 μm.

arrays obtained with two different q-plates working in tuned conditions ($\delta\approx\pi$). SEM images of the arrays by exploiting the q-plates with $q=1$ (top) and $q=2$ (bottom) are illustrated in Figure 10 for two different values of the step scan size Δ. Zoomed views registered at higher magnification of the corresponding SEM images are also given for each case. The SEM images of (A) and (B) report the array elaborated with a step scan size $\Delta\approx100$ μm, almost equal to the spot diameter d. The formed array is made of well-separated annular craters that just touch each other, thus leaving the pristine silicon only as circular discs corresponding to the center of the cater and diamond-shaped regions appearing in the middle of any group of four adjacent spots. Surface structures form inside the annular crater, whose pattern depends on the local state of polarization, while the surface of non-ablated areas of the pristine sample surface is mostly decorated with redeposited nanoparticles. A similar array can be obtained for $q=2$ as shown in (E) and (F) of Figure 10, with the unitary disc characterized by a larger radius associated to the higher topological charge. (C) and (G) of Figure 10 address the possible changes occurring when Δ is reduced to a value smaller than d; in this case, $\Delta\approx80$ μm. In the case of $q=1$, this generates a two-dimensional array of craters that are partially overlapped to each other leaving only the central non-ablated area of each crater, producing a surface morphology made by a periodic array of discs with a diameter of ≈45 μm. A similar condition of overlapped craters in the case of $q=2$, with $\Delta\approx80$ μm, leads to the formation of a secondary pattern of inclined squares with a side of ≈30 μm (as shown in G) due to the partial ablation of the central circular disk by the upcoming pulses. It is worth noticing that a similar approach to the fabrication of large-area arrays formed by repeating annular modified structures on silicon was reported earlier by Fuentes-Edfuf et al. [68]. Different from here, in their work, a Gaussian beam was exploited, and the amorphous micro-rings on crystalline silicon were formed upon melting and rapid solidification

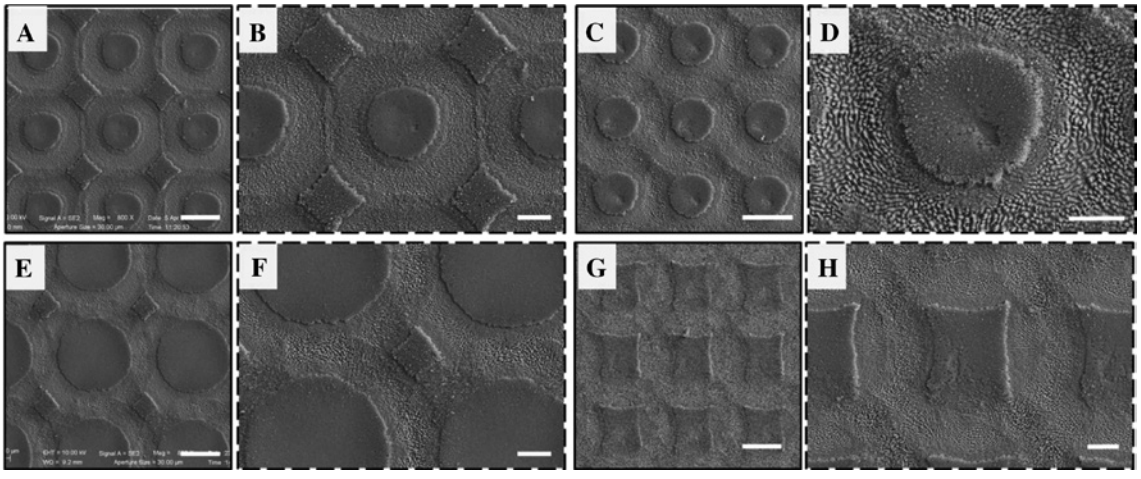

Figure 10: SEM images and zoomed views of the patterns obtained using a VV beam generated by a q-plate in tuned condition ($\delta\approx\pi$) with topological charge $q=1$ and $E\approx20$ μJ (A–D) and $q\approx2$ and $E\approx70$ μJ (E–H). The number of pulses for each elemental crater is set at $N=100$. The nominal step size of the translation stage is (A, E) $\Delta\approx100$ μm, whereas $\Delta\approx80$ μm in the case (C) and (G). The scale bars are (A, C, E, G) 50 μm and (B, D, F, H) 50 μm.

into the amorphous phase of the heated silicon, without surface ablation.

More complex arrays can be formed using as basic tile the more intricated shapes that can be obtained by associating the optical retardation tuning of the q-plate with the step scan approach [69]. This approach can allow patterning the sample surface with a plurality of symmetrical and asymmetrical individual features with diverse shapes and orientations of the craters, thanks to the facile, voltage-driven control of the retardation tuning of the q-plate and by inserting an optical element allowing an easy rotation of the direction of the linear polarization of the input laser beam. By such an approach, a variety of surface patterns can be possibly achieved by exploiting the versatility offered by the variation of beam size and step scan parameters, the polarization of the input beam, the proper selection of topological charge q, and optical retardation δ of the q-plate.

6 Conclusions

In summary, we presented a review of experimental findings obtained using complex VV laser beams with an fs pulse duration generated by a q-plate. The properties of these laser beams being characterized by spatially variant polarization and fluence distributions can allow generating laser-induced periodic surface structures with a large variety of patterns, going from the simpler azimuthal, radial, and spiral ones achieved by exploiting a q-plate with topological charge $q=1/2$, to very complex textures in which ripples and grooves curl around following the local polarization of the complex light beam for VV beams generated by a q-plate with larger q-values. Moreover, the voltage driving of the q-plate allows elaborating beams with asymmetric structures formed by superimposition of the input Gaussian field and the VV field generated by the q-plate in tuned conditions. This possibility adds a further knob to laser structuring as it allows realizing craters with peculiar shapes and surface textures with intriguing patterns. Other examples of the versatility of the method were addressed by presenting the possibilities offered by polarization filtering to create multi-spot surface patterns and step scan fabrication approach to replicate basic shapes forming arrays of structures over larger areas. Though direct fs laser surface processing with complex light beams is still a rather young research field, we expect that the related activities and applications will rapidly advance in the years ahead. In such a context, our experimental findings testify the versatility of an approach based on complex light fields generated by q-plates that can provide a feasible way to design unconventional surface patterns and fabricate more complex surfaces with novel or extended functionalities.

Acknowledgments: We would like to thank R. Fittipaldi and A. Vecchione of the 'Multifunctional Materials Synthesis and Analysis' (MUSA) laboratory of CNR-SPIN and F. Cardano, L. Marrucci, D. Paparo, and A. Rubano of the 'Physics of Structured Light And Matter and of their interaction' (SLAM) group at the Department of Physics, University of Naples 'Federico II', for their contributions. R. Bruzzese is also acknowledged for the fruitful discussions.

References

[1] A. Y. Vorobyev and C. Guo, Laser Photonics Rev. 7, 385 (2013).
[2] J. Bonse, S. Hoehm, S. V. Kirner, A. Rosenfeld and J. Krueger, IEEE J. Sel. Top. Quantum Electron. 23, 9000615 (2017).
[3] F. A. Müller, C. Kunz and S. Gräf, Materials (Basel). 9, 476 (2016).
[4] M. Malinauskas, A. Žukauskas, S. Hasegawa, Y. Hayasaki, V. Mizeikis, et al., Light Sci. Appl. 5, e16133 (2016).
[5] M. Duocastella and C. B. Arnold, Laser Photon. Rev. 6, 607 (2012).
[6] R. Stoian, M. K. Bhuyan, G. Zhang, G. Cheng, R. Meyer, et al., Adv. Opt. Technol. 7, 165 (2018).
[7] J. Secor, R. Alfano and S. Ashrafi, in 'Complex Light' (IOP Publishing, Bristol, UK, 2017).
[8] F. Cardano and L. Marrucci, Nat. Photonics 9, 776 (2015).
[9] J. P. Torres and L. Torner, in 'Twisted Photons: Applications of Light With Orbital Angular Momentum' (Wiley-VCH Verlag GhbH & Co. KGaA, Weinheim, Germany, 2011).
[10] L. Marrucci, E. Karimi, S. Slussarenko, B. Piccirillo, E. Santamato, et al., J. Opt. 13, 064001 (2011).
[11] Q. Zhan, Adv. Opt. Photonics 1, 1 (2009).
[12] H. Rubinsztein-Dunlop, A. Forbes, M. V. Berry, M. R. Dennis, D. L. Andrews, et al., J. Opt. 19, 013001 (2017).
[13] S. Pancharatnam, Proc. Indian Acad. Sci. – Sect. A 44, 398 (1956).
[14] J. N. Ross, Opt. Quantum Electron. 16, 455 (1984).
[15] F. D. M. Haldane, Phys. Rev. Lett. 59, 1788 (1987).
[16] D. Pohl, Appl. Phys. Lett. 20, 266 (1972).
[17] J.-F. Bisson, J. Li, K. Ueda and Y. Senatsky, Opt. Express 14, 3304 (2006).
[18] T. Erdogan, O. King, G. W. Wicks, D. G. Hall, E. H. Anderson, et al., Appl. Phys. Lett. 60, 1921 (1992).
[19] C. Tamm and C. O. Weiss, Opt. Angular Momentum 7, 1034 (1990).
[20] M. W. Beijersbergen, L. Allen, H. E. L. O. van der Veen and J. P. Woerdman, Opt. Commun. 96, 123 (1993).
[21] V. Y. Bazhenov, M. V. Vasnetsov and M. S. Soskin, J. Expt. Theor. Phys. Lett. 52, 429 (1990).
[22] M. W. Beijersbergen, R. P. C. Coerwinkel, M. Kristensen and J. P. Woerdman, Opt. Commun. 112, 321 (1994).

[23] M. Beresna, M. Gecevičius and P. G. Kazansky, Opt. Mater. Express 1, 783 (2011).
[24] N. R. Heckenberg, R. Mcduff, C. P. Smith and A. G. White, in 'Generation of Optical Phase Singularities by Computer-Generated Holograms' (OSA, Washington, DC, United States 1992).
[25] L. Marrucci, C. Manzo and D. Paparo, Phys. Rev. Lett. 96, 163905 (Massachusetts Ave., N.W. Washington, D.C. 20036-1012 USA, 2006).
[26] F. Cardano, E. Karimi, S. Slussarenko, L. Marrucci, C. de Lisio, et al., Appl. Opt. 51, C1 (2012).
[27] M. Huang, F. Zhao, Y. Cheng, N. Xu and Z. Xu, ACS Nano 3, 4062 (2009).
[28] G. D. Tsibidis, M. Barberoglou, P. A. Loukakos, E. Stratakis and C. Fotakis, Phys. Rev. B 86, 115316 (2012).
[29] H. Zhang, J.-P. Colombier, C. Li, N. Faure, G. Cheng, et al., Phys. Rev. B 92, 174109 (2015).
[30] T. J. Y. Derrien, T. E. Itina, R. Torres, T. Sarnet and M. Sentis, J. Appl. Phys. 114, 083104 (2013).
[31] J. Bonse, M. Munz and H. Sturm, J. Appl. Phys. 97, 013538 (2005).
[32] G. D. Tsibidis, C. Fotakis and E. Stratakis, Phys. Rev. B – Condens. Matter Mater. Phys. 92, 041405 (2015).
[33] G. D. Tsibidis, E. Skoulas, A. Papadopoulos and E. Stratakis, Phys. Rev. B 94, 081305 (2016).
[34] G. D. Tsibidis, A. Mimidis, E. Skoulas, S. V. Kirner, J. Krüger, et al., Appl. Phys. A 124, 27 (2018).
[35] S. He, J. J. Nivas, A. Vecchione, M. Hu and S. Amoruso, Opt. Express 24, 3238 (2016).
[36] S. He, J. J. Nivas, K. K. Anoop, A. Vecchione, M. Hu, et al., Appl. Surf. Sci. 353, 1214 (2015).
[37] J. J. J. Nivas, F. Gesuele, E. Allahyari, S. L. Oscurato, R. Fittipaldi, et al., Opt. Lett. 42, 2710 (2017).
[38] L. L. Ran, S. L. Qu and Z. Y. Guo, Chinese Phys. B 19, 034204 (2010).
[39] C. Hnatovsky, V. G. Shvedov, W. Krolikowski and A. V. Rode, Opt. Lett. 35, 3417 (2010).
[40] W. C. Shen, C. W. Cheng, M. C. Yang, Y. Kozawa and S. Sato, J. Laser Micro Nanoeng. 5, 229 (2010).
[41] C. Hnatovsky, V. Shvedov, W. Krolikowski and A. Rode, Phys. Rev. Lett. 106, 123901 (2011).
[42] C. Hnatovsky, V. G. Shvedov, N. Shostka, A. V. Rode and W. Krolikowski, Opt. Lett. 37, 226 (2012).
[43] J. Hamazaki, R. Morita, K. Chujo, Y. Kobayashi, S. Tanda, et al., Opt. Express 18, 2144 (2010).
[44] K. Toyoda, K. Miyamoto, N. Aoki, R. Morita and T. Omatsu, Nano Lett. 12, 3645 (2012).
[45] K. Toyoda, F. Takahashi, S. Takizawa, Y. Tokizane, K. Miyamoto, et al., Phys. Rev. Lett. 110, 143603 (2013).
[46] K. Lou, S.-X. Qian, X.-L. Wang, Y. Li, B. Gu, et al., Opt. Express 20, 120 (2012).
[47] O. J. Allegre, Y. Jin, W. Perrie, J. Ouyang, E. Fearon, et al., Opt. Express 21, 21198 (2013).
[48] Y. Jin, O. J. Allegre, W. Perrie, K. Abrams, J. Ouyang, et al., Opt. Express 21, 25333 (2013).
[49] J. Ouyang, W. Perrie, O. J. Allegre, T. Heil, Y. Jin, et al., Opt. Express 23, 12562 (2015).
[50] G. D. Tsibidis, E. Skoulas and E. Stratakis, Opt. Lett. 40, 5172 (2015).
[51] M. Alameer, A. Jain, M. G. Rahimian, H. Larocque, P. B. Corkum, et al., Opt. Lett. 43, 5757 (2018).
[52] E. Skoulas, A. Manousaki, C. Fotakis and E. Stratakis, Sci. Rep. 7, 45114 (2017).
[53] K. K. Anoop, A. Rubano, R. Fittipaldi, X. Wang, D. Paparo, et al., Appl. Phys. Lett. 104, 241604 (2014).
[54] K. K. Anoop, R. Fittipaldi, A. Rubano, X. Wang, D. Paparo, et al., J. Appl. Phys. 116, 113102 (2014).
[55] B. Piccirillo, V. D'Ambrosio, S. Slussarenko, L. Marrucci and E. Santamato, Appl. Phys. Lett. 97, 241104 (2010).
[56] A. Rubano, F. Cardano, B. Piccirillo and L. Marrucci, J. Opt. Soc. Am. B 36, D70 (2019).
[57] A. D'Errico, M. Maffei, B. Piccirillo, C. de Lisio, F. Cardano, et al., Sci. Rep. 7, 40195 (2017).
[58] J. J. J. Nivas, S. He, A. Rubano, A. Vecchione, D. Paparo, et al., Sci. Rep. 5, 17929 (2015).
[59] E. Karimi, B. Piccirillo, L. Marrucci and E. Santamato, Opt. Lett. 34, 1225 (2009).
[60] G. Vallone, A. Sponselli, V. D'Ambrosio, L. Marrucci, F. Sciarrino, et al., Opt. Express 24, 16390 (2016).
[61] O. Varlamova, M. Bounhalli and J. Reif, Appl. Surf. Sci. 278, 62 (2013).
[62] J. J. J. Nivas, E. Allahyari, F. Gesuele, P. Maddalena, R. Fittipaldi, et al., Appl. Phys. A 124, 198 (2018).
[63] J. J. J. Nivas, E. Allahyari, F. Cardano, A. Rubano, R. Fittipaldi, et al., Sci. Rep. 8, 13613 (2018).
[64] J. J. Nivas, K. K. Anoop, R. Bruzzese, R. Philip and S. Amoruso, Appl. Phys. Lett. 112, 121601 (2018).
[65] J. J. J. Nivas, S. He, Z. Song, A. Rubano, A. Vecchione, et al., Appl. Surf. Sci. 418, 565 (2017).
[66] A. A. Kuchmizhak, A. P. Porfirev, S. A. Syubaev, P. A. Danilov, A. A. Ionin, et al., Opt. Lett. 42, 2838 (2017).
[67] J. J. Nivas, F. Cardano, Z. Song, A. Rubano, R. Fittipaldi, et al., Sci. Rep. 7, 42142 (2017).
[68] Y. Fuentes-Edfuf, M. Garcia-Lechuga, D. Puerto, C. Florian, A. Garcia-Leis, et al., Appl. Phys. Lett. 110, 211602 (2017).
[69] J. J. J. Nivas, E. Allahyari, F. Cardano, A. Rubano, R. Fittipaldi, et al., Appl. Surf. Sci. 471, 1028 (2019).